Article

Phase-homogeneous mixed-halide perovskites for stable tandem photovoltaics

https://doi.org/10.1038/s41586-026-10929-2

Received: 14 December 2025

Accepted: 19 July 2026

Published online: 27 July 2026

Check for updates

Pengju Shi[1,2,8], Jiale Zhuang[1,8], Dayong Zhang[1,8], Chu Li[1,2,8], Stefan Zeiske[1,2], Jin Hou[1,2], Isaiah W. Gilley[1], Ilhan Yavuz[3], Ubaid Kazianga[1], Congqi Li[1,2], Yu Zhang[1,2], Kefu Huang[1], Teerapat Itsoponpan[1,2], Xin Jiang[1,2], Chiung-Han Chen[1,2], Chuying Huang[1], Yi Yang[1,2], Xianfu Zhang[1,2], Pronoy Nandi[1,2], Samantha A. Reitz[1], Antonio Facchetti[1,4], Keith P. White[5], Keenan W. Wyatt[5], Michael F. Toney[5,6,7], Mercouri G. Kanatzidis[1], Tobin J. Marks[1]✉, Cheng Liu[1,2]✉, Bin Chen[1,2]✉ & Edward H. Sargent[1,2]✉

Mixed-halide wide-bandgap (WBG) perovskites needed in tandem photovoltaics suffer from phase segregation, even at the time of initial film formation: the result of asymmetric nucleation of I-rich and Br-rich phases[1–3]. Known homogenization strategies tune Pb^{2+} coordination strength[4–6]; however, Pb^{2+}-based modulation applies across all Pb^{2+} centres and does not preferentially address the problem that $PbBr_x$ nucleates faster than does PbI_x. Here we introduce a selective coordination principle: we tune local Lewis-base hardness at the donor atom through a molecular dipole, an approach that constrains the polarizability of the oxygen donor's outermost electrons. The harder oxygen donor preferentially coordinates the harder Pb^{2+} of $PbBr_x$, selectively retarding Br-rich nucleation and synchronizing it with PbI_x. This leads to compositionally homogeneous WBG films, enabling solar cells with bandgaps of 1.62 eV, 1.68 eV and 1.88 eV, each achieving enhanced power conversion efficiency and extended stability (1,500 hours, $\geq T_{90}$, 1 sun and 65 °C). Perovskite–organic tandem cells fabricated with these WBG films and an infrared-active organic cell deliver certified 27.0% (steady-state 26.4%) efficiency, with T_{91} (ISOS-L2 at 65 °C) of 1,000 hours.

Stacking mixed-halide wide-bandgap (WBG) perovskite solar cells (PSCs) atop narrow-bandgap subcells, such as organic photovoltaics[7–10], copper indium gallium selenide[11–13], lead tin perovskite[14–16] and crystalline silicon[17–19], provides tandem solar cells having power conversion efficiencies (PCEs) higher than those available in single-junction architectures[20–22]. However, the operating stability of these tandem photovoltaics remains an issue because WBG absorbers are particularly prone to phase segregation[2,3].

From a materials synthesis perspective, this segregation process begins at the time of nucleation during initial materials processing[1], and it is then further exacerbated by light-induced later-stage ion migration[23,24]. The initial phase segregation originates from asymmetric nucleation between I-based and Br-based perovskites: the smaller Br^- radius intensifies the Pb^{2+} electrostatic field, fostering stronger interactions within the $PbBr_x$ A-site framework and accelerating the crystallization of Br-rich domains[1].

In seeking synthetic routes to a more homogeneous crystallization process, researchers have tuned the strength of Pb^{2+} coordination through two routes. Indirect approaches include A-site engineering (oleylammonium[4], rubidium[5] and imidazolium alloying[6]), acting by means of nuclei-surface capping, lattice strain and mixing entropy, influencing nucleation without selectively modulating the Pb^{2+} first-coordination sphere that governs phase selection. Direct routes, using Lewis-base modulation[1,25–29], introduce donor ligands that bind Pb^{2+} in competition with the coordinating solvent in the Pb-solvent-halide precursor complex[25], with additives selected through the Pb–ligand interaction strength.

These bond strength-based coordination approaches do not select for $PbBr_x$ relative to PbI_x, because both share the same Pb^{2+} centre having the same frontier orbitals, and differ only in their local halide-dependent environment (Supplementary Figs. 1–4). Previous Lewis-base strategies optimize ligands for the magnitude of the Pb–ligand interaction, and this scales in the same fashion across the Pb^{2+} centres, rather than targeting faster-nucleating $PbBr_x$ relative to PbI_x. The asymmetric nucleation of Br-rich and I-rich phases therefore persists. The strategies do moderate the rate of nucleation at low Br content, but they do not resolve the high-Br regime (50%), wherein severe phase segregation creates grain boundaries and interfacial defects that facilitate ion migration and that compromise device stability[30].

We reasoned that to resolve this asymmetry would require not merely a stronger coordination ligand, but a more selective one: one providing differential coordination within a Pb-centred system sensitive to

[1]Department of Chemistry, Northwestern University, Evanston, IL, USA. [2]Department of Electrical and Computer Engineering, Northwestern University, Evanston, IL, USA. [3]Department of Physics, Marmara University, Istanbul, Türkiye. [4]School of Materials Science and Engineering, Georgia Institute of Technology, Atlanta, GA, USA. [5]Materials Science & Engineering, University of Colorado Boulder, Boulder, CO, USA. [6]Department of Chemical and Biological Engineering, University of Colorado Boulder, Boulder, CO, USA. [7]Renewable and Sustainable Energy Institute, University of Colorado Boulder, Boulder, CO, USA. [8]These authors contributed equally: Pengju Shi, Jiale Zhuang, Dayong Zhang, Chu Li. ✉e-mail: t-marks@northwestern.edu; cheng.liu@northwestern.edu; bin.chen@northwestern.edu; ted.sargent@northwestern.edu

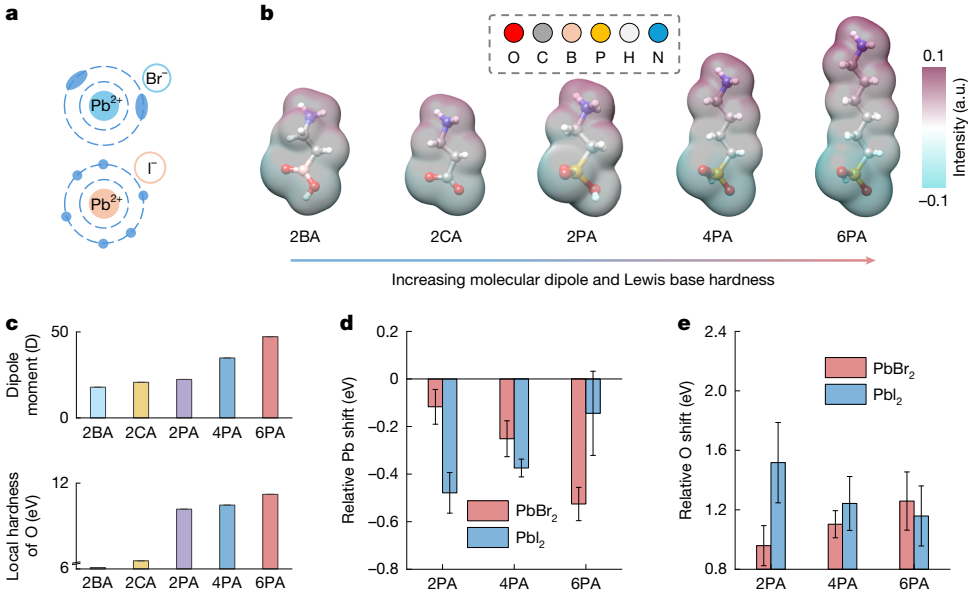

Fig. 1 | Selective coordination of organic Lewis bases to PbI_x and $PbBr_x$. **a**, Schematic illustration of Lewis acidity hardness for Pb in PbI_x and $PbBr_x$. **b**, Molecular structures and electrostatic potentials of 2BA, 2CA, 2PA, 4PA and 6PA. **c**, Calculated dipole moments and local hardness (larger local hardness corresponds to a small softness) of the oxygen atom for each molecule. **d**,**e**, Statistical analysis of XPS binding energy shifts for Pb $4f_{7/2}$ (**d**) and O 1*s* (**e**) after coordination with 2PA, 4PA and 6PA, relative to uncoordinated PbI_x and $PbBr_x$ films. Each condition for the statistics has seven XPS data. a.u., arbitrary units.

halide-induced local perturbation, rather than a global coordination strength. Here we explore local Lewis-base hardness[31] at the donor atom (oxygen or O-donor) as a path to selectivity, an approach offering fine coordination resolution at the level of local charge density.

We achieve this tuning of local electrostatics through the molecular dipole moment, an approach that constrains the polarizability of the outermost electrons of the O-donor. The concept connects to local hard–soft acid–base theory: at an interacting atomic site, binding is maximized when local hardness values match[32,33]. A harder O-donor, achieved by hardness modulation (HM), preferentially coordinates the harder Pb^{2+} in $PbBr_x$ (ref. 32), selectively retarding the faster-nucleating $PbBr_x$ and synchronizing its nucleation with PbI_x to provide compositionally homogeneous WBG perovskite films.

Selective coordination with Pb in $PbBr_2$

We began by examining the local chemical environment of Pb in $PbBr_2$ and PbI_2 with the aid of X-ray photoelectron spectroscopy (XPS) (Supplementary Fig. 5). $PbBr_2$ shows a higher Pb $4f_{7/2}$ binding energy (139.0 eV) than PbI_2 (138.5 eV), indicating a lower valence electron density of Pb in $PbBr_2$ than in PbI_2, reflecting greater Lewis acid hardness[31–33] (Fig. 1a). We pursued harder Lewis bases for their propensity to coordinate preferentially with Pb in $PbBr_2$.

We modulated the local hardness of the O-donor Lewis base by tailoring its local electrostatic environment, a process achieved by tuning molecular dipole moments with varying electron-donating groups and alkyl chain architectures. To this end, we used a series of molecules differing in terminal functional groups and chain lengths, which included 2-aminoethylboronic acid (2BA), 3-aminopropionic acid (2CA), 2-aminoethylphosphonic acid (2PA), 4-aminobutylphosphonic acid (4PA) and 6-aminohexylphosphonic acid (6PA) (Fig. 1b). The calculated dipole moments range from 17.8 D for 2BA to 20.7 D for 2CA and 22.4 D for 2PA (Fig. 1c and Supplementary Note 1). The increase in dipole moments induces a more localized electronic distribution on the O atom, resulting in a gradual and consistent enhancement in local Lewis-base hardness (or reduced local softness) of the O-donor as the chelating anchoring group evolves from boronic to carboxylic to phosphonic acid[34–37] (Fig. 1c). Extending the alkyl chain length of phosphonic acid derivatives further increased this hardness, with 6PA showing the larger dipole and/or increased localized hardness (47.2 D, 11.5 eV), followed by 4PA (34.9 D, 11.1 eV) and 2PA (22.4 D, 10.9 eV).

To probe solution-state interactions, we performed ^{207}Pb nuclear magnetic resonance on $FA_{0.8}Cs_{0.2}PbI_3$ and $FA_{0.8}Cs_{0.2}PbBr_3$ precursors[38]. As O-donor hardness increased from 2PA to 6PA, the ^{207}Pb signal of the $PbBr_x$ precursor shifts relatively from −3.90 ppm and −2.18 ppm to +1.12 ppm, whereas that of the PbI_x precursor shifts relatively less, from −4.93 ppm and −2.85 ppm to +0.41 ppm (Supplementary Figs. 6 and 7), indicating preferential coordination of 6PA with $PbBr_x$. This trend is consistent with XPS: for PbI_x-based films, the Pb $4f_{7/2}$ shift decreases from −0.48 eV to −0.37 eV and −0.14 eV, whereas for $PbBr_x$-based films it increases from −0.12 eV to −0.25 eV and −0.53 eV; the O 1*s* shifts showed the same divergence (Fig. 1d,e, Supplementary Figs. 8–13 and Supplementary Table 1). These results support a local hard–soft acid–base-guided coordination preference at the level of local charge density of 6PA towards $PbBr_x$ over PbI_x (Supplementary Note 2).

Achieving initial phase homogeneity

Selective coordination is expected to induce competitive interaction with $PbBr_x$ between 6PA and A-site cations during nucleation. This competition could raise the nucleation kinetics barrier in the Br-based perovskite phase, inhibiting nucleation and growth rate to match more closely with those of PbI_x-rich systems (Fig. 2a).

We used in situ grazing-incidence wide-angle X-ray scattering (GIWAXS) during spin coating to track the real-time formation of perovskite films with bandgaps of 1.62 eV, 1.68 eV and 1.88 eV. Control 1.62 eV perovskite films (Fig. 2b) show no detectable (100) diffraction peaks before antisolvent deposition. As the Br content increased, these diffraction peaks emerged earlier in the 1.68 eV and 1.88 eV WBG perovskites, respectively (Fig. 2c,d). Thus, increasing Br incorporation accelerates nucleation kinetics. The 1.68 eV control perovskite showed two (100) peaks: one at low scattering vector (Q) (10.0 nm^{-1}) and one at high Q (10.4 nm^{-1}) (Fig. 2c). The high-Q (100) peak at 10.4 nm^{-1} corresponds to a Br-rich phase, and the low-Q peak at 10.0 nm^{-1} is from

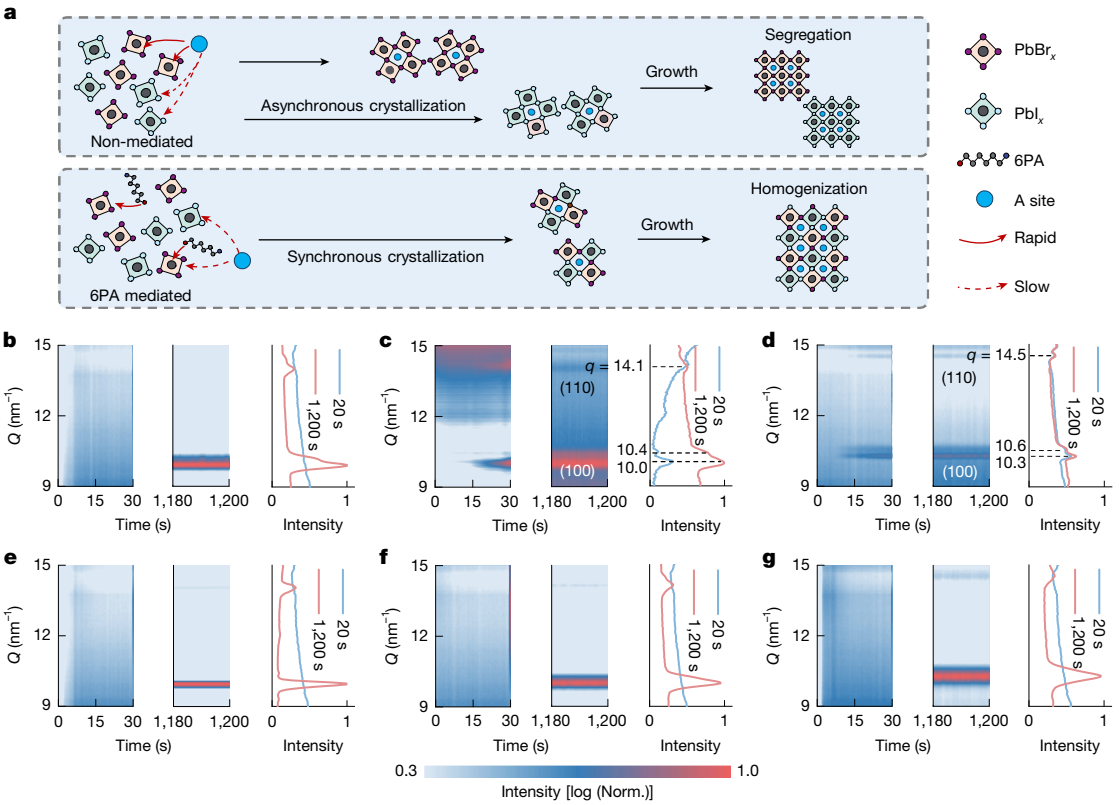

Fig. 2 | Selective modulation of crystallization through a HM strategy. **a**, Schematic illustration of crystallization in WBG perovskite films with and without the HM strategy. **b**–**g**, In situ GIWAXS measurements of perovskite films of the control at 1.62 eV (**b**), control at 1.68 eV (intensity, 0.1–1.0 for 0–30 s), (**c**) control at 1.88 eV (**d**), HM at 1.62 eV (**e**), HM at 1.68 eV and (**f**) HM at 1.88 eV (**g**). Chlorobenzene antisolvent was dropped at 30 s and spin coated to 1,200 s under an active nitrogen purge. The corresponding line profiles at 20 s and 1,200 s are shown to the right of each two-dimensional image, with mixed phases highlighted by dashed black lines in the 1.68 eV and 1.88 eV WBG films.

the target mixed-halide composition, showing phase segregation during crystallization. This segregation becomes more pronounced in the 1.88 eV control perovskite, which showed evident peak splitting in the (100) peak even before antisolvent deposition, forming low-Q (10.3 nm^{-1}) and high-Q (10.6 nm^{-1}) phases attributable to the target and Br-rich compositions, respectively (Fig. 2d).

By contrast, films prepared using the local HM approach show delayed nucleation across compositions, without perovskite diffraction emerging before antisolvent deposition (Fig. 2e–g). In addition, the ultra-WBG (1.88 eV) film shows more homogeneous formation of the targeted perovskite phase throughout the crystallization process with minimum secondary phases. These results further indicate that the local HM strategy with 6PA compensates for the activation-energy divergence[39], consistent with the improved initial phase homogeneity (Supplementary Note 3 and Supplementary Fig. 14).

HM strategy also preserves phase homogeneity throughout annealing, evidenced by well-defined and symmetric X-ray diffraction reflections across the 1.62–1.88 eV range (Supplementary Fig. 15). This increased homogeneity is also seen in the halide distribution over the vertical extent of the 1.62–1.88 eV perovskite films (Supplementary Fig. 16). By contrast, the 1.88 eV control shows broad, asymmetric peaks with secondary features[40,41], indicating residual phase heterogeneity within the final films. The HM strategy yields WBG perovskite films with enhanced crystallinity and suppressed non-radiative recombination (Supplementary Figs. 17 and 18).

Target phase retained after ageing

From ultraviolet–visible (UV–vis) light optical absorption spectra, the HM strategy does not substantially alter the optical bandgap of perovskite films (Supplementary Fig. 19 and Supplementary Table 2). The phase distribution of films was probed by confocal photoluminescence mapping. Spatially resolved photoluminescence mapping of control perovskite films shows progressively increased emission-energy heterogeneity as the bandgap widens from 1.62 eV to 1.88 eV, with the variance rising from 3.1 to 16.9 (Fig. 3a–c). By contrast, films fabricated by means of the HM strategy show more uniform photoluminescence emission across bandgaps. Phase evolution under continuous 1-sun illumination was further examined. HM-based films showed enhanced retaining of targeted phase across all bandgaps, whereas control films develop increasingly redshifted phases with widening bandgap, indicative of enhanced phase segregation. These findings were also corroborated with the aid of electroluminescence measurements under a 2-V bias (Supplementary Fig. 20).

Previous studies have also established a direct correlation between phase segregation and the formation of defect states[42,43]. High-dynamic-range external quantum efficiency (HDR-EQE) measurements enabled us to investigate defects by examining the sub-band tails (Supplementary Fig. 21). To avoid low-finesse optical cavity effects that can introduce apparent sub-bandgap features and obscure defect-related absorption, we fabricated control and HM-treated devices with the same total stack thicknesses. We then monitored the HDR-EQE response of 1.62 eV, 1.68 eV and 1.88 eV WBG PSCs, with and without the HM strategy, during accelerated ageing under continuous 1-sun equivalent illumination at 65 °C under open-circuit conditions. The HDR-EQE is plotted as a function of photon energy and compared for different ageing times between 0 h (fresh device; dark coloured lines) and 96 h (light coloured lines)[44]. The defect density is calculated from the integrated sub-gap EQE, where the integrated area serves as a relative measure of trap density under the assumption

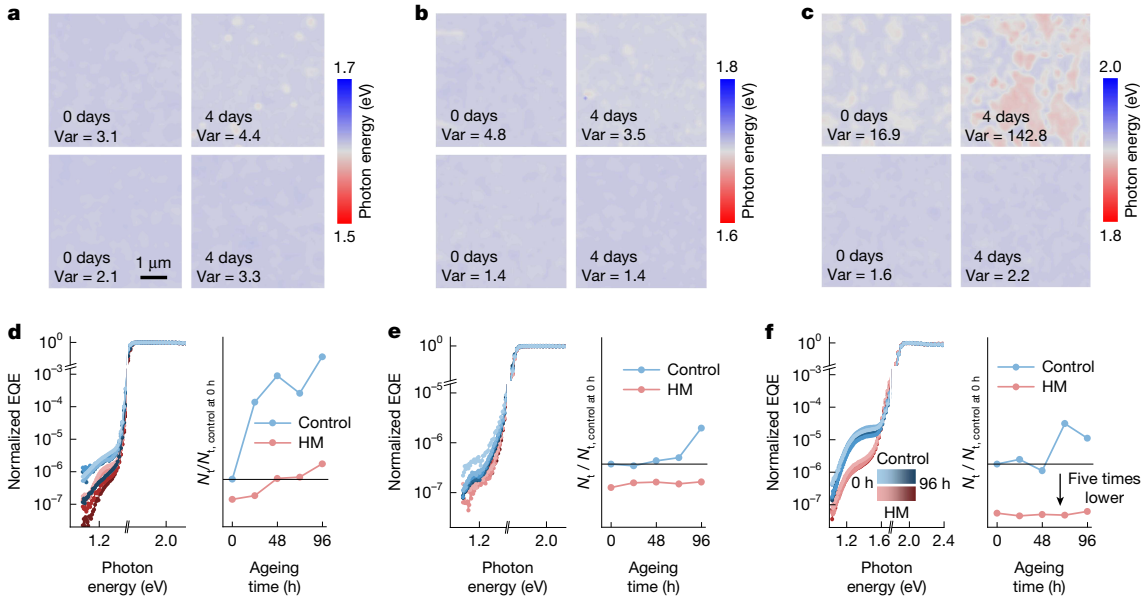

Fig. 3 | Perovskite film functional homogeneity. a–c, Photoluminescence emission maps of perovskite films with bandgaps of 1.62 eV (**a**), 1.68 eV (**b**) and 1.88 eV (**c**), prepared with or without the HM strategy and recorded before and after 4 days of ageing (scale, 5 × 5 μm²). The variance, var, is noted in the bottom-left of each sub-panel. **d–f**, Normalized EQE and defect densities after 0 h, 24 h, 48 h, 72 h and 96 h of continuous 1-sun illumination at 65 °C for 1.62 eV (**d**), 1.68 eV (**e**) and 1.88 eV (**f**) PSCs fabricated with and without the HM strategy.

of constant device thickness (and thus comparable interference effects).

Phase segregation already present at time $t = 0$ in control perovskites is indicated by higher defect densities across all bandgaps, and this increases further, in line with the observed degradation (Fig. 3d–f). In particular, the control 1.88 eV perovskite, the most initially compositionally inhomogeneous, shows a pronounced rise in defect density following ageing. Films prepared using the HM strategy maintain their initial phase homogeneity, showing negligible variation in defect density (remaining fivefold lower) and a consistently reduced initial defect level.

Photovoltaic performance and stability

We evaluated the performance and stability of the resulting perovskite films with different bandgaps by integrating them into devices. Single-junction devices using the HM strategy achieve PCEs of 25.1%, 24.6% and 18.9% for 1.62 eV, 1.68 eV and 1.88 eV WBG PSCs, respectively. Hysteresis is low, and these PCEs outperform control counterparts at 24.2%, 23.6% and 17.6%. The trends are consistent with the stabilized power output results (Supplementary Figs. 22–24 and Supplementary Tables 3–5). The enhancements are statistically notable (Fig. 4a and Supplementary Figs. 25–28) and dominated by increases in both fill factor and open-circuit voltage (V_{oc}). This strategy is also effective in 1 cm² devices, with champion efficiencies of 24.3%, 23.8% and 18.2% (Supplementary Figs. 29–33 and Supplementary Table 6).

The impact of selectively modulated crystallization on device stability was further investigated for single-junction photovoltaic devices (Fig. 4b). Single-junction devices with bandgaps of 1.62 eV, 1.68 eV and 1.88 eV were subjected to continuous 1-sun illumination under open-circuit conditions at 65 °C and roughly 40% relative humidity. After around 1,500 hours of operation, the devices using the HM strategy retain 95%, 94% and 90% of their initial PCEs. By contrast, control PSCs show a pronounced PCE decline after only 200 h, retaining 70%, 44% and 33% of their initial efficiencies for the respective bandgaps. These results are consistent with maximum power point-tracking stability data under ISOS-L1 and ISOS-L2 (65 °C) protocols (Supplementary Figs. 34 and 35). Under a more rigorous ageing protocol (1 sun, 90 °C), the 1.88 eV WBG PSCs using the HM strategy showed superior open-circuit stability (Fig. 4c). In stark contrast to the control devices, which plummeted to 30% of their initial PCE, the HM-based PSCs preserve 85% of their efficiency after 528 h, confirming their robustness under high-temperature and light-soaking stress. We also used electroluminescence spectroscopy to evaluate phase segregation in WBG devices following stability tests (Supplementary Fig. 36). PSCs processed using the HM strategy maintain single-phase emission after ageing, even at elevated temperatures (65 °C) and humidity (roughly 40%). In sum, the HM strategy suppresses ion migration, as seen in reduced ionic conductivity, increased activation energy and enhanced bias-dependent stability across WBG compositions 1.62–1.88 eV (Supplementary Figs. 37–39).

We integrated the 1.88 eV WBG perovskite into perovskite–organic tandem devices (Supplementary Fig. 40). The organic solar cell was selected to provide spectral complementarity and bandgap matching with the 1.88 eV WBG perovskite; based on PM6, BTPSe-Ph4F and MO-IDIC-2F, it provides an efficiency of 19.2%, making it suited for being the bottom cell in perovskite–organic tandems (Supplementary Figs. 41 and 42 and Supplementary Table 7). As seen in Supplementary Fig. 43, both V_{oc} and fill factor improve, and the average PCE across 24 devices also increases with the HM strategy. The best-performing tandem device achieves a PCE of 28.1%, with a fill factor of 83.4%, V_{oc} of 2.19 V and J_{sc} of 15.4 mA cm^{-2} (Fig. 4d and Supplementary Fig. 44). The stabilized power output PCE was 27.8% (Supplementary Fig. 45). These results are retained when we scale tandem devices from 0.05 cm² to 1 cm², with the HM strategy leading to a champion PCE of 27.3% (Supplementary Figs. 46 and 47).

The efficiency of these perovskite–organic tandem solar cells was certified by the National Photovoltaic Industry Measurement and Testing Center, yielding a certified PCE of 27.0%, a record for perovskite–organic tandem technology (Fig. 4e and Supplementary Figs. 48–50). Certified EQE spectra (Supplementary Fig. 51) also reveal well-matched integrated J_{sc} values between the constituent subcells.

Light-cycling stability was also evaluated under cyclic illumination, in which the light intensity was increased to 1 sun for 1 h, maintained for 11 h, reduced to dark for 1 h and then held in the dark for 11 h. The HM-based tandem solar cells retain 90% of their initial PCE after 42 cycles (more than 1,000 h) (Supplementary Fig. 52). For validation, the encapsulated

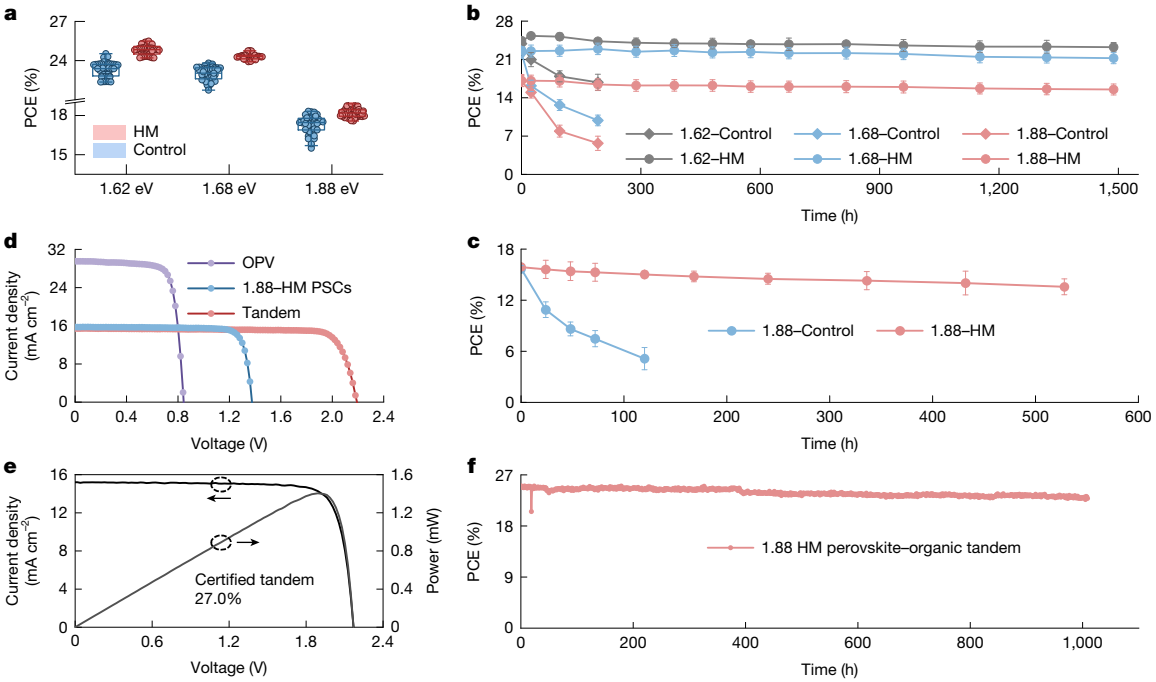

Fig. 4 | Investigation of performance of single-junction and tandem devices. a, Statistical PCEs of 1.62 eV, 1.68 eV and 1.88 eV WBG PSCs with and without using the HM strategy (50 samples each condition). **b**, Stability of 1.62 eV, 1.68 eV and 1.88 eV single-junction PSCs measured under open-circuit conditions at 65 °C, ~40% relative humidity and 1 sun (mean value ± s.d.). **c**, Open-circuit stability of 1.88 eV single-junction PSCs at 90 °C and 1 sun in an N_2 glovebox (mean value ± s.d). **d**, Current density–voltage (J–V) curve of the best-performing perovskite–organic tandem solar cell. OPV, organic photovoltaic. **e**, Certified J–V curve of perovskite–organic tandem solar cells. **f**, Stability of encapsulated perovskite–organic tandem solar cells under ISOS-L2 protocols (65 °C; 1 sun) in air.

perovskite–organic tandem solar cells were aged under continuous 1-sun illumination following ISOS-L2 (65 °C) protocols with PCE tracked under maximum power point conditions. The tandem device fabricated using the HM strategy retains 91% of its initial PCE after 1,000 h under ISOS-L2 (65 °C, Fig. 4f and Supplementary Figs. 53 and 54), an encouraging operating stability among perovskite–organic tandem solar cells reported to date (Supplementary Table 8). Electroluminescence spectra of the aged perovskite–organic tandem solar cell also reveal no signs of secondary phase formation in the HM sample (Supplementary Fig. 55).

Discussion

Hard Lewis bases preferentially coordinate to the harder Lewis-acidic Pb sites in $PbBr_x$, enabling balanced crystallization kinetics of WBG perovskites. This harmonizes nucleation and growth, preserves phase purity and suppresses segregation across a WBG range, yielding high PCEs and operating stability under light and heat stress. These findings position local hardness of Lewis bases as promising candidates for tailoring WBG perovskite crystallization towards enhanced performance and durability in tandem optoelectronics.

Online content

Any methods, additional references, Nature Portfolio reporting summaries, source data, extended data, supplementary information, acknowledgements, peer review information; details of author contributions and competing interests; and statements of data and code availability are available at https://doi.org/10.1038/s41586-026-10929-2.

1. An, Y. et al. Optimizing crystallization in wide-bandgap mixed halide perovskites for high-efficiency solar cells. *Adv. Mater.* **36**, 2306568 (2024).
2. Zhang, Z. et al. Suppression of phase segregation in wide-bandgap perovskites with thiocyanate ions for perovskite/organic tandems with 25.06% efficiency. *Nat. Energy* **9**, 592–601 (2024).
3. Du, L. et al. Photo-homogenization assisted segregation easing technique (PHASET) for highly efficient and stable wide-bandgap perovskite solar cells. *Nat. Commun.* **16**, 8080 (2025).
4. Chen, Y. et al. Nuclei engineering for even halide distribution in stable perovskite/silicon tandem solar cells. *Science* **385**, 554–560 (2024).
5. Zheng, L. et al. Strain-induced rubidium incorporation into wide-bandgap perovskites reduces photovoltage loss. *Science* **388**, 88–95 (2025).
6. Chen, M. et al. Regulating the crystallization of mixed-halide perovskites by cation alloying for perovskite-organic tandem solar cells. *Energy Environ. Sci.* **17**, 9580–9589 (2024).
7. Jia, Z. et al. Efficient near-infrared harvesting in perovskite-organic tandem solar cells. *Nature* **643**, 104–110 (2025).
8. Jiang, X. et al. Isomeric diammonium passivation for perovskite-organic tandem solar cells. *Nature* **635**, 860–866 (2024).
9. Chen, W. et al. Monolithic perovskite/organic tandem solar cells with 23.6% efficiency enabled by reduced voltage losses and optimized interconnecting layer. *Nat. Energy* **7**, 229–237 (2022).
10. Brinkmann, K. O. et al. Perovskite-organic tandem solar cells. *Nat. Rev. Mater.* **9**, 202–217 (2024).
11. Pei, F. et al. Inhibiting defect passivation failure in perovskite for perovskite/Cu(In,Ga)Se_2 monolithic tandem solar cells with certified efficiency 27.35%. *Nat. Energy* **10**, 824–835 (2025).
12. Tian, W. et al. Inert interlayer secures flexible monolithic perovskite/CIGS tandem solar cells with efficiency beyond 21%. *ACS Energy Lett.* **10**, 562–568 (2025).
13. Tian, L. et al. Divalent cation replacement strategy stabilizes wide-bandgap perovskite for Cu(In,Ga)Se_2 tandem solar cells. *Nat. Photonics* **19**, 479–485 (2025).
14. Lin, R. et al. All-perovskite tandem solar cells with dipolar passivation. *Nature* **648**, 600–606 (2025).
15. Gao, H. et al. Homogeneous crystallization and buried interface passivation for perovskite tandem solar modules. *Science* **383**, 855–859 (2024).
16. Tong, J. et al. Carrier lifetimes of >1 µs in Sn-Pb perovskites enable efficient all-perovskite tandem solar cells. *Science* **364**, 475–479 (2019).
17. Wu, W. et al. Stable and uniform self-assembled organic diradical molecules for perovskite photovoltaics. *Science* **389**, 195–199 (2025).
18. Aydin, E. et al. Pathways toward commercial perovskite/silicon tandem photovoltaics. *Science* **383**, eadh3849 (2024).
19. Liu, J. et al. Efficient and stable perovskite-silicon tandem solar cells through contact displacement by MgF_x. *Science* **377**, 302–306 (2022).
20. Shi, P. et al. Oriented nucleation in formamidinium perovskite for photovoltaics. *Nature* **620**, 323–327 (2023).
21. Park, J. et al. Controlled growth of perovskite layers with volatile alkylammonium chlorides. *Nature* **616**, 724–730 (2023).
22. Liu, C. et al. Bimolecularly passivated interface enables efficient and stable inverted perovskite solar cells. *Science* **382**, 810–815 (2023).

23. Wen, J. et al. Present status of and future opportunities for all-perovskite tandem photovoltaics. *Nat. Energy* **10**, 681–696 (2025).
24. Xu, J. et al. Triple-halide wide-band gap perovskites with suppressed phase segregation for efficient tandems. *Science* **367**, 1097–1104 (2020).
25. Yang, W. S. et al. High-performance photovoltaic perovskite layers fabricated through intramolecular exchange. *Science* **348**, 1234–1237 (2015).
26. Ye, Q. et al. Competitive crystallization modulated phase-homogeneous wide-bandgap perovskites for monolithic perovskite-organic tandem solar cells. *Adv. Mater.* **37**, e11781 (2025).
27. Yeom, K. W., Lee, D. K. & Park, N. G. Hard and soft acid and base (HSAB) engineering for efficient and stable Sn-Pb perovskite solar cells. *Adv. Energy Mater.* **12**, 2202496 (2022).
28. Meng, Y. et al. Tailoring colloidal precursor chemistry for tunable nucleation kinetics in all-perovskite tandem solar cells. *Joule* **10**, 102381 (2026).
29. Hu, S. et al. Accessing metal-containing species in tin-lead perovskite precursor solutions via molecular strategies guided by the hard-soft acid-base principle. *Angew. Chem. Int. Ed.* **137**, e202514010 (2025).
30. McMeekin, D. P. et al. Intermediate-phase engineering via dimethylammonium cation additive for stable perovskite solar cells. *Nat. Mater.* **22**, 73–83 (2023).
31. Fukui, K. Role of frontier orbitals in chemical reactions. *Science* **218**, 747–754 (1982).
32. Pearson, R. G. Hard and soft acids and bases. *J. Am. Chem. Soc.* **85**, 3533–3539 (1963).
33. Pearson, R. G. Hard and soft acids and bases, HSAB, part II: underlying theories. *J. Chem. Educ.* **45**, 643 (1968).
34. Parr, R. G. & Yang, W. Density functional approach to the frontier-electron theory of chemical reactivity. *J. Am. Chem. Soc.* **106**, 4049–4050 (1984).
35. Geerlings, P., De Proft, F. & Langenaeker, W. Conceptual density functional theory. *Chem. Rev.* **103**, 1793–1874 (2003).
36. Yang, W. & Parr, R. G. Hardness, softness, and the Fukui function in the electronic theory of metals and catalysis. *Proc. Natl Acad. Sci. USA* **82**, 6723–6726 (1985).
37. Ayers, P. W. & Parr, R. G. Variational principles for describing chemical reactions: the Fukui function and chemical hardness revisited. *J. Am. Chem. Soc.* **122**, 2010–2018 (2000).
38. Cho, S.-H. et al. Solution-phase PbI_2 coordination controls perovskite film formation and photovoltaic performance. *ACS Energy Lett.* **10**, 3931–3940 (2025).
39. Liang, Z. et al. Homogenizing out-of-plane cation composition in perovskite solar cells. *Nature* **624**, 557–563 (2023).
40. Shen, X. et al. Crystal-facet-directed all-vacuum-deposited perovskite solar cells. *Nat. Mater.* **25**, 999–1010 (2026).
41. Li, N. et al. Cation and anion immobilization through chemical bonding enhancement with fluorides for stable halide perovskite solar cells. *Nat. Energy* **4**, 408–415 (2019).
42. Ridzoňová, K. et al. Correlating light-induced deep defects and phase segregation in mixed-halide perovskites. *J. Mater. Chem. A* **10**, 18928–18938 (2022).
43. van Gorkom et al. Revealing defective interfaces in perovskite solar cells from highly sensitive sub-bandgap photocurrent spectroscopy using optical cavities. *Nat. Commun.* **13**, 349 (2022).
44. Othman, M. et al. Alleviating nanostructural phase impurities enhances the optoelectronic properties, device performance and stability of cesium-formamidinium metal–halide perovskites. *Energy Environ. Sci.* **17**, 3832–3847 (2024).

Publisher's note Springer Nature remains neutral with regard to jurisdictional claims in published maps and institutional affiliations.

Springer Nature or its licensor (e.g. a society or other partner) holds exclusive rights to this article under a publishing agreement with the author(s) or other rightsholder(s); author self-archiving of the accepted manuscript version of this article is solely governed by the terms of such publishing agreement and applicable law.

© The Author(s), under exclusive licence to Springer Nature Limited 2026

Methods

Materials

(4-(3,6-Dimethyl-9*H*-carbazol-9-yl)butyl)phosphonic acid (Me-4PACz), PbI_2 (99.99%) and $PbBr_2$ (99.99%) were purchased from TCI America. Formamidinium iodide and propane-1,3-diammonium iodide ($PDAI_2$) were purchased from Greatcell Solar Materials. C_{60} was purchased from Xi'an Yuri Solar Co. Ltd. CsI (99.99%), *N*,*N*-dimethylformamide (DMF, anhydrous, 99.8%), dimethyl sulfoxide (DMSO, anhydrous, 99.9%), isopropanol (anhydrous, 99.5%), ethanol (anhydrous, 99.5%), chlorobenzene (anhydrous, 99.8%), 2-aminoethylphosphonic acid, 4-aminobutylphosphonic acid and hydrochloride 6-aminohexylphosphonic acid were purchased from Millipore Sigma. The PM6, BTPSe-Ph4F and MO-IDIC-2F were purchased from Solarmer Beijing, Inc. All the materials were used as received without any purification. The 2PA·HCl and 4PA·HCl were synthesized (Supplementary Figs. 56 and 57). Then, 100 mg of 2PA or 4PA was dissolved in 2 ml of hydrochloric acid in a round-bottom flask under stirring. The solvent was removed by rotary evaporation, yielding a sticky brownish residue, which was then transferred to a mortar and triturated with excess diethyl ether. White precipitates formed upon grinding were collected by vacuum filtration and dried in an oven.

Fabrication of PSCs

Self-assembled monolayers were used as the hole transport layer: (4-(3,6-dimethyl-9*H*-carbazol-9-yl)butyl)phosphonic acid (Me-4PACz) was used in ethanol at 0.5 mg ml^{-1}. (4-(9′-Phenyl-9*H*,9′*H*-(3,3′-bicarbazol)-9-yl)butyl) phosphonic acid (4PABCZ) was used at 0.5 mg ml^{-1} for stability test. 1.62 eV ($Cs_{0.2}FA_{0.8}Pb(Br_{0.1}I_{0.9})_3$), 1.68 eV ($Cs_{0.2}FA_{0.8}Pb(Br_{0.22}I_{0.78})_3$) and 1.88 eV ($Cs_{0.2}FA_{0.8}Pb(Br_{0.5}I_{0.5})_3$) perovskite precursors were dissolved in a mixed DMF and DMSO solvent (4:1 v:v) at a concentration of 1.2 M with 5 µl of H_2O added later. The perovskite precursor solution was stirred at room temperature for 30 min and filtered using a 0.2-µm polytetrafluoroethylene membrane before use. The perovskite using the HM strategy was fabricated with introducing 0.5 mg, 1 mg and 1.5 mg 6PA in the 1.62 eV, 1.68 eV and 1.88 eV perovskite precursors. For the passivation, 1 mg $PDAI_2$ was dissolved in 1 ml of isopropyl alcohol solvent that was used only for efficiency. The solution was stirred at room temperature overnight and filtered before use. Indium-tin-oxide (ITO) substrates were cleaned sequentially using detergent, deionized water, acetone and isopropanol, each for 15 min in an ultrasonic bath, followed by UV ozone treatment in ambient air for 30 min. NiO_x was spin coated on the substrates in the air at 4,500 rpm for 25 s, then the self-assembled monolayer was spin coated in a N_2 glovebox at 4,000 rpm for 20 s, followed by annealing at 110 °C for 20 min. The perovskite precursor solutions were filtered and spin-coated to form films at 1,000 rpm for 5 s (acceleration rate 1,000 rpm s^{-1}) and 5,000 rpm for 50 s (acceleration rate 5,000 rpm s^{-1}), respectively. At the last 25 s, 200 µl of chlorobenzene was dropped as the antisolvent. The films were then annealed at 110 °C for 20 min. $PDAI_2$ was dynamically dropped (within 2 s) on the perovskite films at 4,000 rpm for 20 s, followed by annealing at 110 °C for 3 min. The glovebox temperature was maintained at roughly 28 °C, with continuous nitrogen purging throughout the fabrication process. Next, 30 nm (50 nm for elevated-temperature stability) C_{60} was thermally evaporated on the perovskite films under a high vacuum of roughly 10^{-7} Torr. The substrates were then transferred to the atomic layer deposition system (Savannah) to deposit 200 cycles SnO_2 at 90 °C using tetrakis(dimethylamino) tin(IV) and water precursors (H_2O pulse time 0.01 s, waiting time 15 s; Sn pulse time 0.1 s, waiting time 15 s). Finally, 200 nm Cu was thermally evaporated as back electrodes under a high vacuum of roughly 10^{-7} Torr.

Fabrication of tandem solar cell

The perovskite subcell was fabricated as described above before electrode deposition, followed by deposition of Au (1 nm). For fabrication of the organic subcell, a PEDOT:PSS (poly(3,4-ethylenedioxythiophene) polystyrene sulfonate) (diluted to PEDOT:PSS:isopropyl alcohol = 1:3) interlayer was deposited by spin coating (5,000 rpm, 30 s; ACL = 6,000, Laurell WS-650MZ23NPP) from a precursor solution filtered through a 0.45-µm polyvinyl difluoride filter (Millipore Millex-HV), followed by thermal annealing at 105 °C for 7 min. All the above procedures were conducted under ambient conditions. The substrates were then transferred into an argon-filled glovebox for active-layer fabrication. The active-layer solution was prepared by codissolving PM6, BTPSe-Ph4F and MO-IDIC-2F in a weight ratio of 1:1:0.2, with a PM6 concentration of 8 mg ml^{-1}, using *o*-xylene/1-chloronaphthalene (99.5:0.5 v/v) as the solvent mixture. The bulk heterojunction films were spin coated at 2,000 rpm, followed by thermal annealing at 100 °C for 10 min. The PNDIT-F3N interfacial layer was prepared in a methanol solution (1 mg ml^{-1}) with the addition of 0.3 vol% acetic acid, and spin coated at 3,000 rpm. Finally, Ag electrodes (130 nm) were deposited by thermal evaporation through a shadow mask under high vacuum (less than 1×10^{-6} Torr). Stability was measured with a MoO_x–Au inter-recombination layer.

Characterization

The *J*–*V* characteristics were measured at room temperature in an N_2 glovebox using a Keithley 2400 source under simulated AM1.5 G irradiation (100 mW cm^{-2}). The irradiation was achieved using a Xe arc lamp from a Sciencetech A1 Light Line Class AAA solar simulator, which was calibrated with a reference solar cell (Sciencetech SCI-REF-Q) before measurement. No preconditioning was applied to the device before measurement. The scanning step for solar cells was set at 20 mV with a scanning rate of 100 mV s^{-1}. The active areas of the solar cells were defined by opaque metal masks featuring a square aperture with areas of 0.05 cm^2 and 1.022 cm^2. Anti-reflection films were used.

The operational stability test was conducted on encapsulated devices with relative humidity of roughly 40% under 1-sun equivalent illumination (300–1,100 nm) at room temperature and 65 °C (device temperature). The 90 °C (device temperature) stability was measured in an N_2 glovebox. Encapsulation was done by using a capping glass slide sealed with fast drying epoxy (Gorilla 2-Part).

For the XPS instrument, the adventitious carbon peak at 284.8 eV was used to calibrate spectra and mitigate charging effects. Each sample was grounded using copper conductive tape, and charge compensation was performed before each measurement.

EQE spectra were acquired using an Oriel model QE-PV-SI (EnliTech) instrument equipped with a NIST-certified Si diode.

Photoluminescence mapping[45] was performed on a tip-enhanced nano-Raman scattering system integrated with SWIFT and DuoScan technologies. For the variance, the photoluminescence map was divided into 10 × 10 grids, and the average emission position within each grid, E_i, was extracted. Spatial uniformity was then quantified from the variance of these local emission positions across the 100 grids: $\mathrm{Var} = \frac{1}{100}\sum_{i=1}^{100}(E_i - \bar{E})^2$, $\bar{E} = \frac{1}{100}\sum_{i=1}^{100} E_i$. i is the number of grids.

In situ GIWAXS measurements of 1.62 eV and 1.68 eV WBG perovskite were performed on the BL14B beamline and were collected by MarCCD225 detector. The wavelength of X-ray for testing was kept at 1.24 Å and the light incident angle of each sample was kept at 0.5°. In situ GIWAXS of 1.88 eV WBG perovskite data were collected at beamline 11-BM (CMS) at the National Synchrotron Light Source II (NSLS-II). These samples were irradiated at an incidence angle of 0.5° at 12.7 keV and were spin coated under a continuously active nitrogen purge at 5 standard cubic feet per hour. Data were collected with a Pilatus 800k detector, calibration, azimuthal integration and *q*-space mapping were performed using the PyFAI software package[46].

HDR-EQE measurements were performed on WBG PSCs with nominal bandgaps of 1.62 eV, 1.68 eV and 1.88 eV. These devices were exposed to accelerated ageing under continuous illumination at an elevated temperature of 65 °C. HDR-EQE spectra were acquired at regular intervals

throughout the ageing process to monitor changes in sub-bandgap absorption features.

EL spectra were acquired from the devices under electrical bias. A controlled bias voltage was applied using a source measure unit (Keithley 2450). The emitted light was collected with an integrating sphere (Thorlabs, 4P4), and the corresponding spectra were recorded using a QE Pro spectrometer (Ocean Optics).

Nuclear magnetic resonance spectroscopy was performed using a 400 MHz Bruker Avance III HD Nanobay system.

Stability certification was performed by an accredited agency[47], BST Testing (Shenzhen) Co., Ltd. Continuous operation at the maximum power point under 1 sun irradiance, 65 °C and ambient humidity.

Temperature-dependent activation energies were extracted from dark current–voltage–temperature (*I*–*V*–*T*) measurements using the Fluxim PAIOS platform. Devices were characterized from 300 K to 180 K under dark conditions with voltage sweeps from −0.2 V to 1.5 V. Activation energies were obtained by means of Arrhenius analysis of the forward current in the diode regime, evaluated at 1.3 V within the exponential region of the *I*–*V* characteristics.

Ionic conductivity was estimated from impedance measurements illuminated using a white LED at the maximum nominal intensity of the PAIOS system at 1 V over a frequency range of 10 MHz to 10 Hz, using the difference between the series resistance and low-frequency intercepts. The absolute ionic conductivity was calculated as $\sigma(\text{ion}) = L/(R_{(\text{ion})}A)$, where L is the active layer thickness and A is the device area. All capacitance-dependent measurements were performed using the Fluxim PAIOS system.

X-ray diffraction experiments were performed using a sealed-tube Cu X-ray source, equipped with 1D LynxEye detector.

Time-resolved photoluminescence was measured using a picosecond-pulse diode laser (Pico-quant LDH 450) with a roughly 70-ps pulse width and a repetition rate of 20 MHz or 10 MHz, focused on a sample with a ×100 objective lens and a numerical aperture of 0.90. The photoluminescence signal was acquired through the time-correlated single photon counting strobe lock system.

Scanning electron microscopy was carried out on the Field Emission Environment Scanning Electron Microscope from Quattro S.

Cyclic voltammetry measurements were performed on a Bio-Logic SP-150 electrochemical workstation using a conventional three-electrode configuration in N_2-saturated 0.1 M tetra-*n*-butylammonium hexafluorophosphate (n-Bu_4NPF_6) acetonitrile solution at room temperature with a scan rate of 50 mV s^{-1}. A material-coated glassy carbon electrode, a platinum wire and an Ag/Ag^+ electrode were used as the working, counter and reference electrodes, respectively. The Ag/Ag^+ reference electrode was calibrated against the ferrocene/ferrocenium (Fc/Fc^+) redox couple as an external standard. All potentials were referenced to Fc/Fc^+, whose energy level was taken as −4.8 eV relative to the vacuum level. The highest occupied molecular orbital and lowest unoccupied molecular orbital energy levels of the materials were estimated from the oxidation (ox) and reduction (red) potentials derived from the cyclic voltammetry curves according to the highest occupied molecular orbital (eV) = $-(E_{ox} - E_{Fc/Fc+} + 4.8)$ and lowest unoccupied molecular orbital (eV) = $-(E_{red} - E_{Fc/Fc+} + 4.8)$.

Time of flight secondary ion mass spectrometry depth profiling was performed on C_{60}/perovskite/ITO stacks using an IONTOF M6 instrument. Depth profiling was conducted using a Cs^+ sputtering gun operated at 1 keV and 100 nA.

For UV–vis spectroscopy optical absorption measurements and Tauc analysis, UV–vis absorption spectra of the perovskite films were recorded using a PerkinElmer LAMBDA 1050 spectrophotometer. The films were prepared on transparent substrates under the same processing conditions as those used for the corresponding devices. A blank substrate was used as the reference for baseline correction. The absorption spectra were collected over the wavelength range of 300–900 nm. The measured wavelength-dependent absorbance was then used for optical bandgap estimation by Tauc analysis. For the Tauc plot, the wavelength λ was first converted to photon energy $h\nu$ according to $h\nu = 1{,}240/\lambda$, where $h\nu$ is the photon energy in electronvolts and λ is the wavelength in nanometres. For direct-bandgap perovskite films, the Tauc relationship can be expressed as $(\alpha h\nu)^2 = B(h\nu - E_g)$, where α is the absorption coefficient, B is a proportionality constant and E_g is the optical bandgap. The optical bandgap was estimated from the x axis intercept obtained by linearly extrapolating the absorption-edge region of the Tauc plot.

Reporting summary

Further information on research design is available in the Nature Portfolio Reporting Summary linked to this article.

Data availability

All data needed to evaluate the conclusions in the paper are present in the paper or the Supplementary Information. Further data are available from the corresponding authors upon request. All the density functional theory calculations were performed using the open-source ORCA package available from FACCTs at https://www.faccts.de/orca/.

45. Mao, W. et al. Light-induced reversal of ion segregation in mixed-halide perovskites. *Nat. Mater.* **20**, 55–61 (2021).
46. Kieffer, J. & Karkoulis, D. PyFAI, a versatile library for azimuthal regrouping. *J. Phys. Conf. Ser.* **425**, 202012 (2013).
47. Gao, D. et al. Long-term stability in perovskite solar cells through atomic layer deposition of tin oxide. *Science* **386**, 187–192 (2024).

Acknowledgements In situ GIWAXS measurements of the 1.88 eV WBG perovskite were conducted at beamline 11-BM (CMS) of the National Synchrotron Light Source II, a US Department of Energy (DOE) Office of Science User Facility operated for the DOE Office of Science by Brookhaven National Laboratory under contract no. DE-SC0012704; we thank beamline scientist R. Li for support. This work made use of the EPIC (RRID: SCR_026361) and Keck-II (RRID: SCR_026360) facilities of Northwestern University's NUANCE Center, which has received support from the SHyNE Resource, the International Institute for Nanotechnology and Northwestern's MRSEC program. T.J.M. and A.F. acknowledge Office of Naval Research grants N00014-24-1-2109 (Northwestern University) and N00014-24-1-2110 (Georgia Tech.). This material is based upon work supported in part by the National Science Foundation Graduate Research Fellowship Program under grant DGE 2040434.

Author contributions P.S. conceived of the idea, developed the concept, proposed the experimental design and wrote the paper under the supervision of C. Liu, B.C. and E.H.S. D.Z. fabricated the organic photovoltaic subcell, conducted related characterizations and did optical, electronic and structural data analyses under the supervision of T.J.M. and A.F. J.Z. performed materials synthesis, carried out nuclear magnetic resonance, XPS and X-ray diffraction characterizations and conducted data analysis. T.I. and C.-H.C. assisted with 1.88 eV WBG PSCs. J.H., I.Y., U.K., Congqi Li, Y.Z., K.H., X.J., C.H., X.Z., P.N. and S.A.R. assisted with characterizations and device fabrications. S.Z. conducted HDR-EQE and electroluminescence measurements and corresponding analysis. Chu Li conducted density functional theory calculations. K.P.W., K.W. and M.F.T. conducted in situ GIWAXS experiments and data reduction. M.G.K., Y.Y. and I.W.G. contributed to helpful discussions.

Funding This work was supported by the Paula M. Trienens Institute for Sustainability and Energy at Northwestern University. This material is based on work supported by the US DOE's Office of Energy Efficiency and Renewable Energy (EERE) under the Solar Energy Technologies Office (SETO) Award Number DE-EE0010502. Northwestern University's NUANCE Center has received support from the SHyNE Resource (grant no. NSF ECCS-2025633), the International Institute for Nanotechnology and Northwestern's MRSEC program (grant no. NSF DMR-2308691).

Competing interests The authors declare no competing interests.

Additional information

Supplementary information The online version contains supplementary material available at https://doi.org/10.1038/s41586-026-10929-2.

Correspondence and requests for materials should be addressed to Tobin J. Marks, Cheng Liu, Bin Chen or Edward H. Sargent.

Peer review information *Nature* thanks Nam-Gyu Park, Thomas Riedl and the other, anonymous, reviewer(s) for their contribution to the peer review of this work. Peer reviewer reports are available.

Reprints and permissions information is available at http://www.nature.com/reprints.

nature research

Corresponding author(s): Tobin J. Marks, Cheng Liu, Bin Chen, Edward H. Sargent

☐ Initial submission ☐ Revised version ■ Final submission

Solar Cells Reporting Summary

Nature Portfolio wishes to improve the reproducibility of the work that we publish. This form is intended for publication with all accepted papers reporting the characterization of photovoltaic devices and provides structure for consistency and transparency in reporting. Some list items might not apply to an individual manuscript, but all fields must be completed for clarity.

For further information on Nature Research policies, including our data availability policy, see Authors & Referees.

Please check the following details are reported in the manuscript, and provide a brief description or explanation where applicable.

Area of the tested solar cells	■ Yes ☐ No	Report the area of the tested solar cells. 0.05 cm2
Method used to determine the device area	■ Yes ☐ No	Provide a description of the method and state where this information can be found in the text. Metal mask (Methods)

2. Current-voltage characterization

Current density-voltage (J-V) plots in both forward and backward direction	■ Yes ☐ No	See Fig. 4d and Supplementary Fig. 22
Voltage scan conditions	■ Yes ☐ No	Provide a description of the measurement conditions (e.g. scan direction, speed, dwell times). J-V was measured with a speed of 0.02V/s and dwell time of 100 ms (Methods)
Test environment	■ Yes ☐ No	Provide a description of the test conditions (e.g. characterization temperature, atmosphere, humidity). Measued in N2 glovebox, RT (Methods).
Protocol for preconditioning of the device before its characterization	☐ Yes ■ No	No preconditioning of the device was applied before the measurement
Stability of the J-V characteristic	■ Yes ☐ No	Provide a description of the method used. The stability of the J-V characteristic can be verified with time evolution of the maximum power point or with the photocurrent at maximum power point; see ref. 5 for details. Photocurrent at maximum power point (Supplementary Figs. 24 and 45)
Description of the unusual behaviour observed during the characterization	☐ Yes ■ No	Provide a description of hysteresis or any other unusual behaviour observed during the characterization.
Related experimental data	☐ Yes ■ No	Provide a description of the related experimental data.
External quantum efficiency (EQE) or incident photons to current efficiency (IPCE)	■ Yes ☐ No	Provide a description of the technique used. EQE, see in Supplementary Figs. 25 and 51
A comparison between the integrated response under the standard reference spectrum and the response measure under the simulator	■ Yes ☐ No	The Jsc obtained from the J-V characteristics was consistent with the value integrated from EQE spectra

For tandem solar cells, the bias illumination and bias voltage used for each subcell

■ Yes
□ No

Provide a description of the measurement conditions.

No bias voltage but bias illumination was used for EQE measurements (473 and 735 nm)

5. Calibration

Light source and reference cell or sensor used for the characterization

■ Yes
□ No

Provide a description of the light source and reference cell or sensor.

Light source is a Xe arc lamp from a ScienceTech A1 Light Line Class AAA solar simulator , The reference solar cell is from Sciencetech (SCI-REF-0).

Confirmation that the reference cell was calibrated and certified

■ Yes
□ No

Identify the independent certification laboratory.

The light intensity was calibrated by the reference solar cell (SCI-REF-Q) from Sciencetech.

Calculation of spectral mismatch between the reference cell and the devices under test

□ Yes
■ No

Provide a value of the spectral mismatch and/or a description of how it has been taken into account in the measurements.

The Jsc from simulator was calibrated by SCI-REF-0

6. Mask/aperture

Size of the mask/aperture used during testing

■ Yes
□ No

Report the size of the mask/aperature.

0.05 cm2

Variation of the measured short-circuit current density with the mask/aperture area

□ Yes
■ No

Report the difference in the short-circuit current density values measured with the mask and aperture area.

We didn't measure the solar cells with apertures of different sizes

7. Performance certification

Identity of the independent certification laboratory that confirmed the photovoltaic performance

■ Yes
□ No

Identify the independent certification laboratory.

National Photovoltaic Industry Measurement and Testing Center (NPVM)

A copy of any certificate(s)

■ Yes
□ No

Certificate copies should be provided in the Supplementary information. Please state the supplementary item number.

Supplementary Figs. 48, 49 and 51

8. Statistics

Number of solar cells tested

■ Yes
□ No

Report how many solar cells have been tested, specifying the number of individual substrates.

50 per condition for single-junction and 24 for tandem devices

Statistical analysis of the device performance

■ Yes
□ No

Fig. 4a, Supplementary Figs. 26-28 and 43

9. Long-term stability analysis

Type of analysis, bias conditions and environmental conditions

■ Yes
□ No

Provide a description of the type of analysis, bias conditions and environmental conditions (e.g. illumination type, temperature, atmosphere humidity, encapsulation method, preconditioning temperature, bias) for each long-term stability analysis carried out; see ref. 7 and 8 for details.

See methods, Fig. 4b, c and f, Supplementary Figs. 34-35

1. Shrotriya, V. *et al*. Accurate measurement and characterization of organic solar cells. *Adv. Funct. Mater.* **16**, 2016–2023 (2006).
2. Dennler, G. *et al*. The value of values. *Mat. Today* **10**, 56 (2007).
3. Cravino, A., Schilinsky, P. & Brabec, C. J. Characterization of organic solar cells: the importance of device layout. *Adv. Funct. Mater.* **17**, 3906–3910 (2007).
4. Reese, M. O. *et al*. Consensus stability testing protocols for organic photovoltaic materials and devices. *Sol. Energ. Mat. Sol. C* **95**, 1253–1267 (2011).
5. Snaith H. .J. The perils of solar cell efficiency measurements. *Nat. Photon*. **6**, 337–340 (2012).
6. Luber, E. J. & Buriak, J. M. Reporting performance in organic photovoltaic devices. *ACS Nano* **7**, 4708–4714 (2013).
7. Snaith, H. J. *et al*. Anomalous hysteresis in perovskite solar cells. *J. Phys. Chem. Lett.* **5**, 1511–1515 (2014).
8. Grätzel M. The light and shade of perovskite solar cells. *Nat. Mat*. **13**, 838–842 (2014).
9. Zimmermann E. *et al*. Erroneous efficiency reports harm organic solar cell research. *Nat. Photon*. **8**, 669–672 (2014).
10. Beard M.C., Luther J.M. & Nozik A.J. The promise and challenge of nanostructured solar cells. *Nat. Nanotech*. **9**, 951–954 (2014).
11. Timmreck, R. *et al*. Characterization of tandem organic solar cells. *Nat. Photon.* **9**, 478–479 (2015).

A number of international committees develop industry standards on the characterization of photovoltaic technologies (for example ASTM-E44 and IEC-TC 82), which can provide guidance for academic research.

This checklist template is licensed under a Creative Commons Attribution 4.0 International License, which permits use, sharing, adaptation, distribution and reproduction in any medium or format, as long as you give appropriate credit to the original author(s) and the source, provide a link to the Creative Commons license, and indicate if changes were made. The images or other third party material in this article are included in the article's Creative Commons license, unless indicated otherwise in a credit line to the material. If material is not included in the article's Creative Commons license and your intended use is not permitted by statutory regulation or exceeds the permitted use, you will need to obtain permission directly from the copyright holder. To view a copy of this license, visit http://creativecommons.org/licenses/by/4.0/